

Fluid–Structure Interaction Modeling of Patient-Specific Cerebral Aneurysms

Kenji Takizawa and Tayfun E. Tezduyar

Abstract We provide an overview of the special techniques developed earlier by the Team for Advanced Flow Simulation and Modeling (T★AFSM) for fluid–structure interaction (FSI) modeling of patient-specific cerebral aneurysms. The core FSI techniques are the Deforming-Spatial-Domain/Stabilized Space–Time formulation and the stabilized space–time FSI technique. The special techniques include techniques for calculating an estimated zero-pressure arterial geometry, a special mapping technique for specifying the velocity profile at an inflow boundary with non-circular shape, techniques for using variable arterial wall thickness, mesh generation techniques for building layers of refined fluid mechanics mesh near the arterial walls, a recipe for pre-FSI computations that improve the convergence of the FSI computations, techniques for calculation of the wall shear stress and oscillatory shear index, and arterial-surface extraction and boundary condition techniques. We show, with results from earlier computations, how these techniques work. We also describe the arterial FSI techniques developed and implemented recently by the T★AFSM and present a sample from a wide set of patient-specific cerebral-aneurysm models we computed recently.

K. Takizawa (✉)

Department of Modern Mechanical Engineering and Waseda Institute for Advanced Study,
Waseda University, 1-6-1 Nishi-Waseda, Shinjuku-ku, Tokyo 169-8050, Japan
e-mail: Kenji.Takizawa@tafsm.org

T. E. Tezduyar

Mechanical Engineering, Rice University, 6100 Main Street, Houston, TX 77005, USA
e-mail: tezduyar@rice.edu

1 Introduction

Arterial fluid mechanics computations involve a number of challenges. One of the major computational challenges is accurate and efficient modeling of the fluid–structure interactions (FSI) between the blood flow and arterial walls. The preferred method of handling the moving interfaces involved in FSI modeling has mostly been the Arbitrary Lagrangian–Eulerian (ALE) finite element formulation (Hughes et al. 1981). One of the earliest space–time formulations targeting FSI modeling is the Deforming-Spatial-Domain/Stabilized Space–Time (DSD/SST) formulation (Tezduyar 1992). The DSD/SST formulation was introduced by the Team for Advanced Flow Simulation and Modeling (T★AFSM) as a general-purpose interface-tracking (i.e. moving-mesh) technique for computation of flow problems with moving interfaces. The formulation is based on the Streamline-Upwind/Petrov–Galerkin (SUPG) (Brooks and Hughes 1982) and Pressure-Stabilizing/Petrov–Galerkin (PSPG) (Tezduyar 1992) methods.

Patient-specific arterial FSI modeling with the DSD/SST formulation was first reported by Torii et al. in a 2004 journal article (Torii et al. 2004) published by the Japan Society of Mechanical Engineers. Over the years following that, Torii et al. conducted one of the most extensive series of patient-specific arterial FSI modeling of cerebral aneurysms (see Torii et al. 2011) and references therein). The cases studied in these articles by Torii et al. were almost all for middle cerebral arteries, and the geometries were constructed from computed tomography images. In these arterial FSI computations the DSD/SST formulation was used together with the mesh update methods (Johnson and Tezduyar 1994; Tezduyar et al. 1993) developed by the T★AFSM and was implemented with block-iterative coupling (Tezduyar 2004) (see (Tezduyar et al. 2006) for the terminology). The inflow boundary condition used in the computations is a pulsatile velocity profile, which closely represents the measured flow rate during a heartbeat cycle. A brief, chronological review of the computations reported was provided in (Tezduyar et al. 2007b).

New generation DSD/SST formulations, with increased scope, robustness and efficiency, were introduced by the T★AFSM in (Tezduyar and Sathe 2007). The stabilized space–time FSI (SSTFSI) technique, which is based on the new-generation DSD/SST formulations, was also introduced in Tezduyar and Sathe (2007). The SSTFSI technique was extended by the T★AFSM in Takizawa et al. (2010a, b; Tezduyar et al. 2007b, 2008, 2009, 2010) to arterial FSI modeling, with emphasis on arteries with aneurysm. The arterial geometries were approximations to patient-specific image-based geometries, mostly to those reported by Torii et al. A number of special techniques for arterial FSI were developed by the T★AFSM in conjunction with the SSTFSI technique. These include techniques for calculating an estimated zero-pressure (EZP) arterial geometry (Takizawa et al. 2010a, b; Tezduyar et al. 2007a, 2008), a special mapping technique for specifying the velocity profile at an inflow boundary with non-circular shape (Takizawa et al. 2010a), techniques for using variable arterial wall thickness (Takizawa et al. 2010a,

b), mesh generation techniques for building layers of refined fluid mechanics mesh near the arterial walls (Takizawa et al. 2010a, b; Tezduyar et al. 2009), a recipe for pre-FSI computations that improve the convergence of the FSI computations (Tezduyar et al. 2007b, 2008), the Sequentially Coupled Arterial FSI (SCAFSI) technique (Tezduyar et al. 2008, 2007c, 2009, 2010) and its multiscale versions (Tezduyar et al. 2009, 2010), and techniques (Takizawa et al. 2010b) for the projection of fluid–structure interface stresses, calculation of the wall shear stress (WSS) and calculation of the oscillatory shear index (OSI). In FSI modeling of three cerebral artery segments with aneurysm reported by the T★AFSM in Takizawa et al. (2011), the arterial geometries came from 3D rotational angiography (3DRA). In Takizawa et al. (2011), the T★AFSM also addressed the computational challenges related to extraction of the arterial-lumen geometry from 3DRA, generation of a mesh for that geometry, and building a good starting point for the FSI computations. In addition to these computational challenges common to all three cases, the computational challenges encountered in some of these cases individually were addressed in Takizawa et al. (2011).

In this chapter we provide an overview of the special techniques developed earlier by the T★AFSM for space–time FSI modeling of patient-specific cerebral aneurysms and present results from earlier computations. We also describe the arterial FSI techniques developed and implemented recently by the T★AFSM and present a sample from a wide set of patient-specific cerebral-aneurysm models we computed recently. The governing equations and the finite element formulations, including the DSD/SST and SSTFSI techniques, can be found in (Tezduyar et al. 2011). The special FSI techniques are described in Sect. 2. In Sect. 3, we describe how we extract the arterial-lumen geometry from 3DRA and generate the mesh. The fluid (blood) and structure (arterial wall) properties and boundary conditions are given in Sect. 4. The pre-FSI computations are described in Sect. 5. We present the test computations in Sect. 6, and give our concluding remarks in Sect. 7.

2 Special Techniques

2.1 Mapping Technique for Inflow Boundaries

The special mapping technique for inflow boundaries was introduced in Takizawa et al. (2010a). We repeat here from Takizawa et al. (2010a) how the technique works.

Some inflow profiles require the inlet to be circular, however the inlets in many of the geometries we encounter are not circular. Furthermore, as the artery deforms, the inlet shape changes. Thus, even if the inlet is initially circular, it will not remain so. The technique introduced in Takizawa et al. (2010a) to meet this requirement maps the inflow boundaries from non-circular shapes to circular shapes. The actual inflow profile $U(\mathbf{z}, t)$, where \mathbf{z} is the coordinate vector in the inflow plane, is obtained by mapping from a preferred inflow profile $U^P(r, t)$. Here

r is the circular coordinate and $0 \leq r \leq r_B$, where r_B is the average radius of the inflow cross-sectional area, which comes from the image-based data. It is calculated by dividing that area by π and taking the square-root of that.

The technique involves two steps:

1. Map \mathbf{z} to r and calculate a “trial” velocity:

$$r(\mathbf{z}) = \frac{\|\mathbf{z} - \mathbf{z}_C\|}{\|\mathbf{z} - \mathbf{z}_B\| + \|\mathbf{z} - \mathbf{z}_C\|} r_B, \quad (1)$$

$$U^T(\mathbf{z}, t) = U^P(r, t), \quad (2)$$

where subscripts “C” and “B” denote the centroid and the closest boundary, respectively, as shown in Fig. 1, and the superscript “T” stands for “trial”.

2. Adjust the velocity:

$$U(\mathbf{z}, t) = \frac{Q(t)}{\int_{\Gamma_{\text{INFL}}} U^T(\mathbf{z}, t) d\Gamma} U^T(\mathbf{z}, t), \quad (3)$$

where Q is the flow rate and Γ_{INFL} is the discretized inflow area; i.e. the integration area in the finite element space.

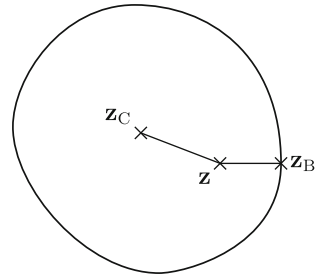
2.2 Wall Shear Stress Calculation

A new technique for calculating the wall shear stress (WSS) was proposed in Takizawa et al. (2010b). We provide the description of the technique from Takizawa et al. (2010b).

We first decompose the spatial version of $(\mathbf{w}_{11}^h)_{n+1}^-$ into its two components:

$$\mathbf{w}_{11}^h = (\mathbf{w}_{11}^h)^W + (\mathbf{w}_{11}^h)^R, \quad (4)$$

Fig. 1 Special mapping technique



where $(\mathbf{w}_{11}^h)^R$ is the part associated with the rim nodes at the lumen ends, and $(\mathbf{w}_{11}^h)^W$ is the part associated with the rest of the fluid mechanics nodes at the arterial wall. We then calculate $(\mathbf{h}_v^h)_{11}$ as follows:

$$\begin{aligned} \int_{\Gamma_h} (\mathbf{w}_{11}^h)^W \cdot (\mathbf{h}_v^h)_{11} d\Gamma &= \int_{\Omega} 2\mu \boldsymbol{\varepsilon} \left((\mathbf{w}_{11}^h)^W \right) : \boldsymbol{\varepsilon}(\mathbf{u}) d\Omega \\ &+ \sum_{e=1}^{(n_{el})_n} \int_{\Omega^e} (\mathbf{w}_{11}^h)^W \cdot \nabla \cdot (2\mu \boldsymbol{\varepsilon}(\mathbf{u})) d\Omega, \end{aligned} \quad (5)$$

$$\int_{\Gamma_h} (\mathbf{w}_{11}^h)^R \cdot ((\mathbf{n} \times \mathbf{e}^R) \cdot \nabla) (\mathbf{h}_v^h)_{11} d\Gamma = 0, \quad (6)$$

where \mathbf{e}^R is the unit vector along the rim.

2.3 Oscillatory Shear Index

The oscillatory shear index (OSI) is a measure of the degree to which WSS oscillates during a heart beat cycle. It is defined (see (Taylor et al. 1998)) as follows:

$$\text{OSI} = \frac{1}{2} \left(1 - \frac{(\mathbf{h}_v^h)_{11}^{\text{NM}}}{(\mathbf{h}_v^h)_{11}^{\text{MN}}} \right), \quad (7)$$

where, following the notation from Takizawa et al. (2010b), “NM” and “MN” stand for “norm of the mean” and “mean of the norm”, and

$$(\mathbf{h}_v^h)_{11}^{\text{NM}} = \frac{1}{T} \left\| \int_0^T (\mathbf{h}_v^h)_{11} dt \right\|, \quad (8)$$

$$(\mathbf{h}_v^h)_{11}^{\text{MN}} = \frac{1}{T} \int_0^T \| (\mathbf{h}_v^h)_{11} \| dt. \quad (9)$$

Here T is the period of the cardiac cycle. Higher OSI indicates larger flow direction variation in a cardiac cycle. As pointed out in Takizawa et al. (2010b), calculating the OSI based on a fixed reference frame is not the best way, because, for example, if an artery segment undergoes rigid-body rotation, that should not influence the OSI. Two methods that exclude rigid-body rotation from the OSI calculation were proposed in Takizawa et al. (2010b).

Method 1

$$(\mathbf{h}_v^h)_{II}^\Delta = \mathbf{J}\mathbf{F}^{-1}(\mathbf{h}_v^h)_{II}, \quad (10)$$

where \mathbf{F} is the deformation gradient tensor associated with the deformation of the fluid–structure interface (not the volumetric deformation gradient of the fluid-domain motion), and $J = \det \mathbf{F}$.

Method 2

$$(\mathbf{h}_v^h)_{II}^\Delta = \mathbf{R}^T(\mathbf{h}_v^h)_{II}, \quad (11)$$

where \mathbf{R} is the rotation tensor coming from the decomposition of \mathbf{F} as

$$\mathbf{F} = \mathbf{R}\mathbf{U}, \quad (12)$$

and \mathbf{U} is the right stretch tensor.

For both methods, $(\mathbf{h}_v^h)_{II}^\Delta$ is calculated as follows:

$$\int_{(\Gamma_{II})_{\text{ROSI}}} \mathbf{w}_{II}^h \cdot (\mathbf{h}_v^h)_{II}^\Delta d\Gamma = \int_{(\Gamma_{II})_{\text{ROSI}}} \mathbf{w}_{II}^h \cdot \mathcal{R}(\mathbf{h}_v^h)_{II} d\Gamma, \quad (13)$$

where $\mathcal{R} = \mathbf{J}\mathbf{F}^{-1}$ or $\mathcal{R} = \mathbf{R}^T$, and $(\Gamma_{II})_{\text{ROSI}}$ is a reference configuration of the fluid–structure interface used in the OSI calculations. In Eqs. (8) and (9), we replace $(\mathbf{h}_v^h)_{II}$ with $(\mathbf{h}_v^h)_{II}^\Delta$.

Remark 1 A similar concept can be found in Green and Naghdi (1976) as the corotated Cauchy stress, $\mathbf{R}^T \boldsymbol{\sigma} \mathbf{R}$.

Remark 2 The OSI calculations reported in this chapter are based on Eq. (10).

Remark 3 As pointed out in Takizawa et al. (2010b), the reference configuration used in Eq. (13) is not necessarily the unstressed configuration of the fluid–structure interface. For the calculations reported in this book chapter, it is the configuration corresponding to the instant when the pressure is at its time-averaged value (on the way up, i.e. at the ascending part of the pressure curve).

3 Arterial Geometry, Mesh Generation and Estimated Zero-Pressure Geometry

3.1 Arterial-Surface Extraction from Medical Images

In our current arterial FSI research the arterial geometries come as voxel data from 3D rotational angiography (3DRA) performed at one of the neuroangiography suites at the Memorial Hermann Hospital at the Texas Medical Center. This is

done on a biplane neuroangiographic unit (Allura FD20/10; Philips Medical System, Best, the Netherlands). Adjusting the contrast ratio for this voxel data allows us to visualize and create a triangular surface mesh using a marching cubes algorithm. The vertices of the surface mesh are then passed through a Gaussian smoothing filter to eliminate any high frequency noise and obtain a smooth surface. At the artery inlets and outlets, we select cutting planes that are approximately perpendicular to the flow direction. As pointed out in (Takizawa et al. 2011), this provides better inflow and outflow planes for specifying the fluid mechanics boundary conditions and is also important for imposing proper slip boundary conditions at the inlets and outlets for the structural mechanics and fluid mesh motion (see Sect. 4.5 in Tezduyar et al. 2011). This entire process is carried out using software originally designed by Warren and McPhail for the purpose of interactively imaging the pulmonary structure of the human lung McPhail and Warren (2008).

3.2 Mesh Generation and Estimated Zero-Pressure Arterial Geometry

We use the arterial lumen geometry as input to ANSYS Meshing Tools to generate a quadrilateral surface mesh. As mentioned in Takizawa et al. (2011), at locations where the arteries have large curvature we use more mesh refinement. Based on the surface mesh, we go through a process of determining the arterial wall thickness, generating a hexahedral structural mechanics mesh for the arterial wall (typically with two layers of elements across the arterial wall), and calculating the estimated zero-pressure (EZIP) arterial geometry Takizawa et al. (2010a, b; Tezduyar et al. 2008).

The concept of EZIP geometry was introduced in Tezduyar et al. (2008). Quite often, the image-based geometries are used as arterial geometries corresponding to zero blood pressure. As pointed out in Tezduyar et al. (2008), it is more realistic to use that image-based geometry as the arterial geometry corresponding to the time-averaged value of the blood pressure. Given that arterial geometry at the time-averaged pressure value, an estimated arterial geometry corresponding to zero blood pressure needs to be constructed. This is where the need for an EZIP arterial geometry comes from. In estimating that geometry, the time-averaged value of the blood pressure, obtained by averaging over a cardiac cycle, is 92 mm Hg.

In Takizawa et al. (2011), different wall-thickness ratios are tried with the zero-pressure shape until, approximately, a 10 % wall-thickness ratio (relative to the diameter of the arterial lumen) is obtained at the inflow. At each iteration, the trial wall-thickness ratio is globally uniform (which comes out to be in the range 12–13 % when the iterations end), but the base length scales for the “patches” are defined individually, with a smooth transition between the patches. The patches are

identified as the regions associated with the inflow trunk, each of the outflow branches, and the aneurysm/bifurcation area. The length scales for the inflow and outflow patches are the lumen diameters at those ends. The length scale for the aneurysm/bifurcation patch is a factor times the lumen diameter at the inflow, where the factor was less than one and varied between the three different patient-specific artery models used in Takizawa et al. (2011). The zero-pressure shape at each EZP iteration is obtained by shrinking the surface mesh generated in the surface-extraction process (see Sect. 3.1) by an amount equal to the trial wall-thickness described above. It was pointed out in Takizawa et al. (2011) that this was a simplified implementation and it was proposed to calculate the shrinking amount not with such direct dependence on the trial wall-thickness, but based on a more sophisticated rule of dependence or based on an independent trial objective.

In Takizawa et al. (2010a, b) and Tezduyar et al. (2010) the EZP geometry was calculated in a simpler way. The zero-pressure shape used at each EZP iteration was simply the surface mesh generated in the surface-extraction process, without any shrinking. The calculation was even simpler in Tezduyar et al. (2008, 2009), where the entire artery segment was treated as a single patch.

Following the calculation of the EZP geometry, the structure is inflated to a pressure corresponding to the pressure at the start of our computation cycle (cardiac cycle). After that, we generate, with ANSYS Meshing Tools, a fluid mechanics surface mesh associated with the inflated arterial-wall structure. Then, using that surface mesh, we generate a desired number of layers of refined fluid mechanics volume mesh near the arterial walls. The rest of the fluid mechanics volume mesh is generated with the T★AFSM automatic mesh generator. Layers of refined fluid mechanics volume mesh near the arterial walls were used in T★AFSM computations as early as the computations reported in Tezduyar et al. (2009), followed by the computations reported in Takizawa et al. (2010a, b, 2011) and Tezduyar et al. (2010).

In Takizawa et al. (2011), the layers of refined mesh have locally variable thickness (with smooth transition between areas of different thickness), because some artery branches have very small diameters. The thickness of the layers of refined mesh is determined basically in the same way as the arterial wall thickness is determined in Takizawa et al. (2011). The layers of refined mesh were generated in a simpler way in Takizawa et al. (2010a, b) and Tezduyar et al. (2009, 2010), where the entire artery segment was treated as a single patch. The number of layers was 6 in Tezduyar et al. (2009), with a progression factor of approximately 1.25, and 4 in Takizawa et al. (2010a, b, 2011) and Tezduyar et al. (2010), with a progression factor of 1.75.

In this book chapter we also present results obtained with new techniques for determining the shrinking amount in the EZP process, the arterial wall thickness, and the thickness of the layers of refined fluid mechanics volume mesh near the arterial walls. These techniques were proposed in Remark 2 of Takizawa et al. (2011). Instead of using (nearly) patch-wise constant values (with a smooth transition between the patches) for the EZP shrinking amounts, the wall thicknesses, and the thickness of the layers of refined mesh, we determine the local

values of all three based on the solution of the Laplace’s equation over the surface mesh covering the lumen. In each of the three cases, the Laplace’s equation is solved with values specified at the inflow and outflow boundaries and for the shrinking amount and wall thickness, as needed,¹ at a set of inter-patch points (i.e. points that are considered to be at the boundaries between the patches). The trial ratios for the shrinking amount and wall thickness are no longer globally uniform but are defined individually for the inflow and outflow boundaries (which still come out to be in the range 12–13 % for the wall thickness when the iterations end), and the values specified at the inter-patch points are not directly related to these ratios. Furthermore, instead of targeting just a 10 % wall-thickness ratio at the inflow, we take some additional considerations into account, such as targeting a 10 % wall-thickness ratio also at the outflow boundaries, targeting a wall-thickness for the aneurysm or a set inter-patch points, reasonableness of the aneurysm size and overall shape, and the mesh quality. The trial shrinking is applied, as needed, in multiple steps, with surface remeshing between the steps. Because the parameter space is wider and the targets are multiple, the process involves more user experience, intuition and judgment. Still, of course, the objective in iterating on the values for the shrinking amount and wall thickness is to have an EZP geometry that after inflation to average pressure gives us a shape that closely resembles the lumen geometry from the 3DRA. We note that the trial ratios specified at the boundaries for the shrinking amount and wall thickness are not independent quantities, but related by the incompressibility constraint. In generating the refined fluid mechanics volume mesh near the arterial walls, the number of layers is 4 and the progression factor is 1.75.

Remark 4 The original version of the technique for calculating an EZP geometry was introduced in a 2007 conference paper (Tezduyar et al. 2007a) and the 2008 journal (Tezduyar et al. 2008) as “a rudimentary technique” for addressing the issue. Newer techniques have been introduced since then, such as the new versions we described above and the approach given in Bazilevs et al. (2010). In the approach given in Bazilevs et al. (2010), the geometry of the vessel is left unchanged and a state of pre-stress is found, which puts the artery in equilibrium with the cardiac-cycle-averaged pressure (and viscous forces). The pre-stress is then directly employed for the blood vessel wall tissue modeling in the FSI computations.

Remark 5 A technique for wall-thickness prescription, based on the solution of the Laplace’s equation over the fluid volume mesh, was developed in Bazilevs et al. (2009). The idea of using the Laplace’s equation over the surface mesh covering the lumen to determine the local values of the EZP shrinking amount, the arterial

¹ In some cases where the outflow diameters significantly differ, the solution obtained from the Laplace’s equation for shrinking amount and wall thickness for the aneurysm/bifurcation area could have an undesirable distribution. The need for specifying values at a set of inter-patch points comes from seeking a better distribution in that area.

wall thickness, and the thickness of the layers of refined mesh was motivated by this earlier wall-thickness determination work.

4 Fluid and Structure Properties and Boundary Conditions

4.1 Fluid and Structure Properties

As it was done for the computations reported in Torii et al. (2004, 2011), the blood is assumed to behave like a Newtonian fluid (see Sect. 2.1 in Tezduyar et al. 2008). The density and kinematic viscosity are set to $1,000 \text{ kg/m}^3$ and $4.0 \times 10^{-6} \text{ m}^2/\text{s}$. The material density of the arterial wall is known to be close to that of the blood and therefore set to $1,000 \text{ kg/m}^3$. The arterial wall is modeled with the continuum element made of hyperelastic (Fung) material. The Fung material constants D_1 and D_2 (from Huang et al. 2001) are $2.6447 \times 10^3 \text{ N/m}^2$ and 8.365, and the penalty Poisson's ratio is 0.45. Cerebral arteries are surrounded by cerebrospinal fluid, and we expect that to have a damping effect on the structural dynamics of the arteries. Therefore we add a mass-proportional damping, which also helps in removing the high-frequency modes of the structural deformation. The damping coefficient η is chosen in such a way that the structural mechanics computations remain stable at the time-step size used. It is $1.5 \times 10^4 \text{ s}^{-1}$.

4.2 Boundary Conditions

At the inflow boundary we specify the velocity profile as a function of time, by using the technique introduced in Takizawa et al. (2010a). Here we describe the technique from (Takizawa et al. 2010a). We use a velocity waveform which represents the cross-sectional maximum velocity as a function of time. Assuming that the maximum velocity occurs at $r = 0$, the artery is rigid and the cross-sectional shape is a perfect circle, we can apply the Womersley (1955) solution as follows:

$$U^P(r, t) = A_0 \left(1 - \left(\frac{r}{r_B} \right)^2 \right) + \sum_{k=1}^N A_k \frac{J_0 \left(\gamma \sqrt{k} i^{\frac{3}{2}} \right) - J_0 \left(\gamma \sqrt{k} \left(\frac{r}{r_B} \right) i^{\frac{3}{2}} \right)}{J_0 \left(\gamma \sqrt{k} i^{\frac{3}{2}} \right) - 1} \exp \left(i 2 \pi k \frac{t}{T} \right), \quad (14)$$

where N is the number of Fourier coefficients (we use $N = 20$), $A_k \in \mathbb{C}$ are the Fourier coefficients of the waveform, T is the period of the cardiac cycle, J_0 is the

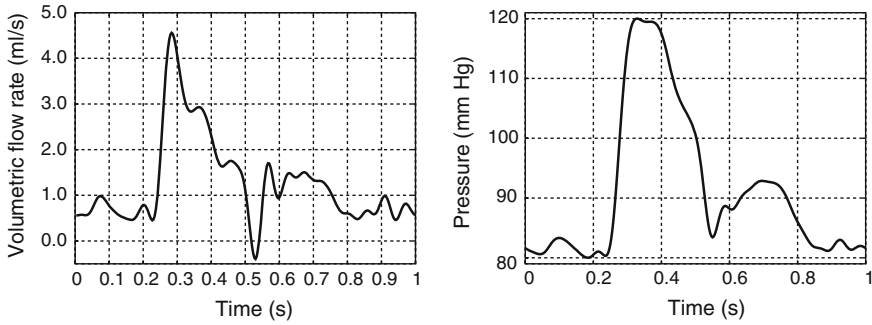


Fig. 2 Sample volumetric flow rate (*left*) and outflow pressure profile (*right*) corresponding to the sample flow rate

Bessel functions of the first kind of order 0, i is the imaginary number, and \mathcal{Y} is the Womersley parameter:

$$\mathcal{Y} = r_B \sqrt{\frac{2\pi}{\nu T}}. \quad (15)$$

We use the special mapping technique described in [Sect. 2.1](#) for non-circular shapes. Figure 2 shows a sample volumetric flow rate as a function of time.

Remark 6. In the current T★AFSM computations, the volumetric flow rate (which was calculated based on a velocity waveform that represents the cross-sectional maximum velocity) is scaled by a factor. The scaling factor is determined in such a way that the scaled flow rate, when averaged over the cardiac cycle, yields a target WSS for Poiseuille flow over an equivalent cross-sectional area. The target WSS is 10 dyn/cm² in the current T★AFSM computations.

At all outflow boundaries of an artery segment, we specify the same traction boundary condition. The traction boundary condition is based on a pressure profile computed as described in (Takizawa et al. 2010a). In that computation, the pressure profile, as a function of time, is determined based on the flow rate and by using the Windkessel model (Frank, 1899). From Eq. (14), we obtain the flow rate as follows:

$$Q(t) = \int_0^{r_B} 2\pi r U^P(r, t) dr \quad (16)$$

$$= \pi r_B^2 \frac{A_0}{2} + \pi r_B^2 \sum_{n=1}^N A_k \frac{J_0(\mathcal{Y} \sqrt{k} t^{\frac{3}{2}}) - 2 \left(\mathcal{Y} \sqrt{k} t^{\frac{3}{2}} \right)^{-1} J_1(\mathcal{Y} \sqrt{k} t^{\frac{3}{2}})}{J_0(\mathcal{Y} \sqrt{k} t^{\frac{3}{2}}) - 1} \exp\left(i 2\pi k \frac{t}{T}\right) \quad (17)$$

$$= \sum_{k=0}^N B_k \exp\left(i2\pi k \frac{t}{T}\right), \quad (18)$$

where J_1 is the Bessel functions of the first kind of order 1, and for notational convenience we introduce another set of coefficients, $B_k \in \mathbb{C}$. The pressure, based on the Windkessel model, can be written as follows:

$$p(t) = \exp\left(-\frac{t}{RC}\right) \int_0^t \frac{1}{C} Q(\tau) \exp\left(\frac{\tau}{RC}\right) d\tau + p_0, \quad (19)$$

where C and R are the compliance and resistance of the distal arterial networks, and p_0 is a constant of integration. Substituting Eq. (18) into Eq. (19), we obtain the following:

$$p(t) = \sum_{k=0}^N \frac{B_k}{i2\pi k \frac{C}{T} + \frac{1}{R}} \left[\exp\left(i2\pi k \frac{t}{T}\right) - \exp\left(-\frac{t}{RC}\right) \right] + p_0. \quad (20)$$

After a sufficient number of periods, the $\exp\left(-\frac{t}{RC}\right)$ term in Eq. (20) goes to 0:

$$p(t) = \frac{T}{C} \sum_{k=0}^N \frac{B_k}{i2\pi k + \frac{T}{RC}} \exp\left(i2\pi k \frac{t}{T}\right) + p_0. \quad (21)$$

Here $\frac{T}{RC}$ is only a profile factor, because it is a parameter that only acts on each Fourier coefficient. We set $\frac{T}{RC}$ to 18.2, and the other parameters, $\frac{T}{C}$ and p_0 , are set in such a way that the range for the pressure profile is from 80 to 120 mm Hg for normal blood pressure. Figure 2 shows the pressure profile corresponding to the sample flow rate.

On the arterial walls, we specify no-slip boundary conditions for the flow. In the structural mechanics part, as boundary condition at the ends of the arteries, we set the normal component of the displacement to zero (see Sect. 4.5 in Tezduyar et al. 2011), and for one of those nodes we also set to zero the tangential displacement component that needs to be specified to preclude rigid-body motion.

5 Simulation Sequence

Recipes for pre-FSI computations that provide a good starting point for the FSI computations and improve their convergence were introduced in Tezduyar et al. (2007b). Now, in all arterial simulations carried out by the T★AFSM, the FSI computations are preceded by a set of pre-FSI computations. These pre-FSI computations include fluid-only and structure-only computations. The recipes introduced in (Tezduyar et al. 2007b) were used also in Tezduyar et al. (2008,

2009). A slightly modified recipe was introduced in Takizawa et al. (2010a), resulting in a simulation sequence called “S \rightarrow F \rightarrow S \rightarrow FSI”, and this is the one that the T★AFSM has been using in its arterial simulations since then.

Structure \rightarrow Fluid \rightarrow Structure \rightarrow FSI (S \rightarrow F \rightarrow S \rightarrow FSI) sequence

Step 1: Generate the structure mesh based on the shape of the unstressed structure.

Step 2: Compute the structural deformation with a uniform fluid pressure held steady at a value close to 80 mm Hg.

- Structural deformation can be determined with a steady-state computation or a time-dependent computation that eventually yields a steady-state solution.
- For the steady-state computation, $\Delta t \rightarrow \infty$ and $\alpha = 0$ in Eq. (23) in Tezduyar et al. (2011), the number of time steps is one, and the initial displacement, velocity and acceleration are set to zero.

Step 3: Generate the fluid mesh based on the shape of the deformed structure.

Step 4: Compute a developed flow field while holding the structure from Step 2 rigid.

- The outflow traction is set to a value close to 80 mm Hg.
- The inflow velocity is set to a value corresponding to the outflow traction.

Step 5: Recompute the structural deformation, with the fluid stresses at the interface held steady at their values from Step 4, and simultaneously update the fluid mesh.

- Structural deformation can be determined with one of the two choices we had in Step 2.

Step 6: Compute the FSI with the same inflow and outflow conditions used in Step 4, with the initial condition for the flow velocity coming from Step 4.

Step 7: Compute the FSI with the inflow and outflow conditions pulsating.

6 Computational Results

All computations were carried out in a parallel computing environment and were completed without any remeshing. The fully discretized, coupled fluid and structural mechanics and mesh-moving equations are solved with the quasi-direct coupling technique (see Sect. 5.2 in Tezduyar and Sathe 2007). In solving the linear equation systems involved at every nonlinear iteration, the GMRES search technique (Saad and Schultz 1986) is used with a diagonal preconditioner.

6.1 WSS Calculations with Refined Meshes

The two different fluid mechanics meshes used in Tezduyar et al. (2010) were a “coarse” mesh with 15,850 nodes and 88,573 four-node tetrahedral elements, and a

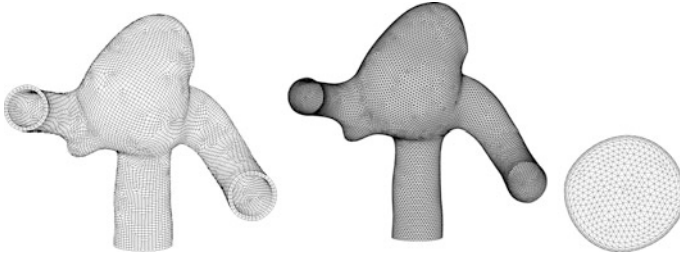


Fig. 3 A bifurcating middle cerebral artery segment with aneurysm. Fine structural mechanics mesh when the outflow pressure is maximum (*left*). Fine fluid mechanics mesh at the fluid–structure interface (*center*) and the inflow plane (*right*)

“medium” mesh with 22,775 nodes and 128,813 four-node tetrahedral elements. The medium mesh has four layers of elements with higher refinement near the arterial wall, with the thickness of the first layer being approximately 0.02 mm. The progression factor is 1.75. The coarse mesh has one layer of elements with a uniform thickness of approximately 0.2 mm. The coarse and medium meshes have the same number of nodes and elements at the fluid–structure interface: 3,057 nodes and 6,052 three-node triangular elements. The computations reported in Takizawa et al. (2010b) were based on the same artery model as the one used in Tezduyar et al. (2010) and involved basically three new features. The new features were (a) carrying out higher-resolution FSI computations with more refined fluid and structure meshes, (b) calculating the WSS with a new technique, as described in Sect. 2.2, and c) reporting OSI values that were calculated with a new technique, as described in Sect. 2.3. We describe the computations from Takizawa et al. (2010b). Two structural mechanics meshes are used. The “coarse” structure mesh consists of 8,067 nodes and 5,316 eight-node hexahedral elements, with 2,689 nodes and 2,658 four-node quadrilateral elements on the fluid–structure interface. The “fine” structure mesh consists of 30,732 nodes and 20,366 eight-node hexahedral elements, with 10,244 nodes and 10,183 four-node quadrilateral elements on the fluid–structure interface and two layers of elements across the arterial wall. It is shown in Fig. 3. The reason behind using a more refined fluid mechanics mesh in the higher-resolution FSI computations reported in Takizawa et al. (2010b) was to increase the accuracy of the WSS calculations by increasing the fluid mechanics mesh refinement also on the arterial wall, not just in the normal direction near the arterial wall. As pointed out in Takizawa et al. (2010b), this would normally make sense only if the structural mechanics mesh has comparable refinement. The refined structural mechanics mesh introduced in Takizawa et al. (2010b), which is shown in Fig. 3, served that purpose. The “fine” fluid mechanics mesh has 138,713 nodes and 823,756 four-node tetrahedral elements. It has 11,713 nodes and 23,304 threenode triangular elements at the fluid–structure interface, which is shown in Fig. 3. The fine mesh, just like the medium mesh, has four layers of elements with higher refinement near the arterial wall. The thickness of the first layer is approximately 0.02 mm and the progression factor is 1.75 (see Fig. 3).

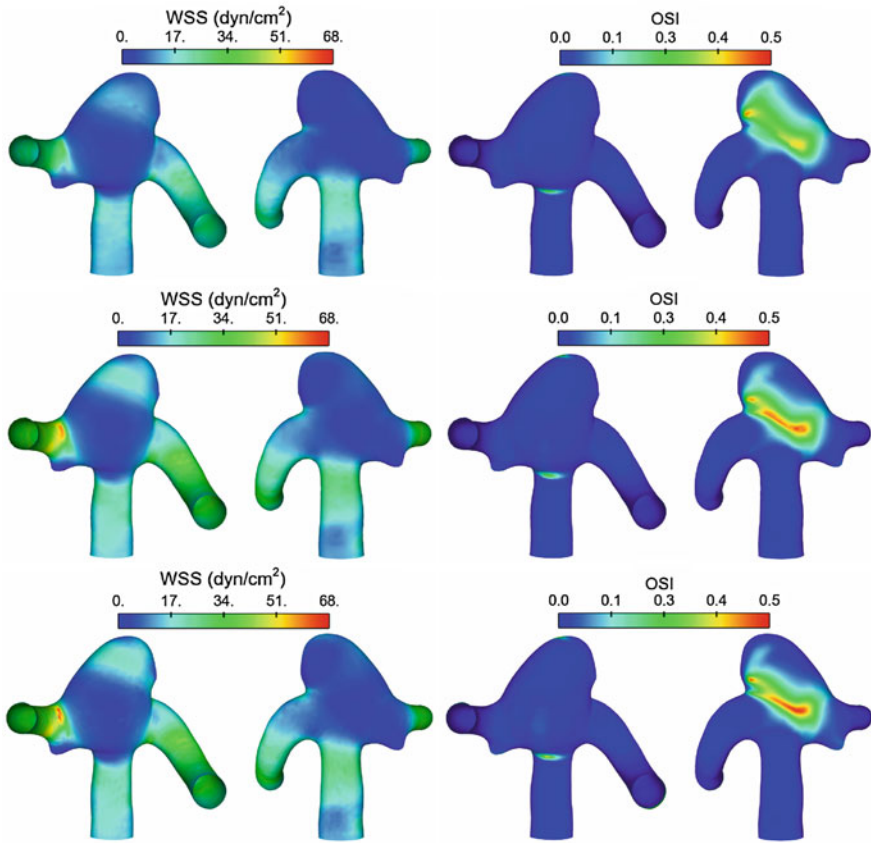


Fig. 4 A bifurcating middle cerebral artery segment with aneurysm. Time-averaged WSS (*left*) and OSI (*right*) for the coarse (*top*), medium (*middle*) and fine (*bottom*) meshes

The computations were carried out with the SSTFSI-TIP1 technique (see Remarks 8 and 16 in (Tezduyar et al. 2011)) and the SUPG test function option WTSA (see Remark 2 in (Tezduyar et al. 2011)). The stabilization parameters used are those given by Eqs. (12)–(18) in Tezduyar et al. (2011). The time-step size is 3.333×10^{-3} s for the coarse and medium meshes and 1.667×10^{-3} s for the fine mesh. For all three meshes the number of nonlinear iterations per time step is 6. For the fluid + structure block the number of GMRES iterations per nonlinear iteration is 300 for the coarse and medium meshes and 600 for the fine mesh. For all six nonlinear iterations the fluid scale is set to 1.0 and the structure scale to 50. For the mesh moving block the number of GMRES iterations is 30. Good mass balance is achieved in all computations. This was verified by comparing the rate of change for the artery volume and the difference between the volumetric inflow and outflow rates. The pictures showing that can be found in Takizawa et al. (2010b). Figure 4 shows, for the three meshes, the time-averaged WSS and the OSI.

Table 1 A bifurcating middle cerebral artery segment with aneurysm

Mesh	Peak systole		Time average		
	Max	Mean	Max	Mean	Min
Coarse	102	37	32	12.53	0.16
Medium	237	54	60	16.76	0.32
Fine	263	53	68	16.53	0.24

WSS (dyn/cm²) for the coarse, medium and fine meshes. Spatial maximum and mean at peak systole, and spatial maximum, mean and minimum of time-averaged values.

Fig. 5 A bifurcating middle cerebral artery segment with aneurysm. Streamlines computed with the fine mesh at $t = 0.268$ s (*left*) and $t = 0.448$ s (*right*). The *streamlines* illustrate the WSS direction changes

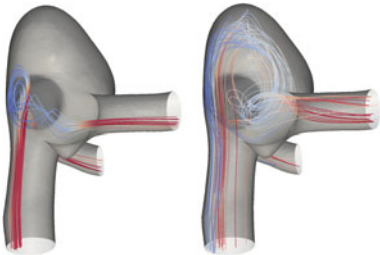


Table 1 shows the maximum, mean and minimum values of the WSS for the three meshes. The higher OSI region indicates flow direction changes over the cardiac cycle. The medium and fine mesh results are in good agreement. Figure 5 shows typical streamlines around the higher OSI region at $t = 0.268$ s (accelerating flow) and $t = 0.448$ s (decelerating flow). When the flow accelerates, a vortex forms, which results in a downward WSS. Conversely, when the flow decelerates, the vortex dissipates and the flow creates an upward WSS. As pointed out in Takizawa et al. (2010b), one of the reasons behind this change in flow characteristics is the motion of the aneurysm. We observe an aneurysm movement towards the left in Fig. 5 when the flow accelerates.

6.2 Computations with the New Techniques for the EZP Geometry, Wall Thickness and Boundary-Layer Element Thickness

We present a sample from a wide set of patient-specific cerebral-aneurysm models used in (Takizawa et al. 2012), where the shrinking amount in the EZP process, the arterial wall thickness, and the thickness of the layers of refined fluid mechanics mesh are determined based on the solution of the Laplace’s equation over the surface mesh covering the lumen (see Sect. 3.2). The length scales used in conjunction with the trial ratios for the inflow and outflow boundaries are the lumen diameters at those ends. The value specified for the thickness of the first layer of

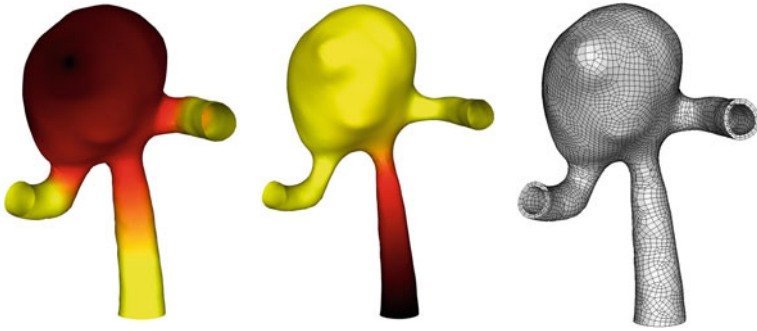


Fig. 6 Model-M6Acom. EZP shrinking amount over the surface (lumen) extracted from the medical image (*left*), wall thickness over the shrunk lumen (*middle*), and structure mesh at zero pressure (*right*). The *color range* represents a value range that increases from *light* to *dark*

elements at the inflow and outflow boundaries is $0.007 \times$ (lumen diameter at those ends). In these computations, the volumetric flow rate is specified by using the scaling technique introduced in Remark 6. Figure 6 shows the EZP shrinking amount, wall thickness, and structure mesh for the arterial model, which we call Model-M6Acom. The diameter of the arterial lumen is 3.13 mm at the inflow end, and 2.12 and 2.11 mm at the outflow ends. The structure mesh has two layers of elements across the arterial wall. For the layers of refined fluid mechanics mesh near the arterial wall, the progression factor is 1.75. Figure 7 shows the fluid mechanics mesh at the lumen, thickness of the first layer of elements near the arterial wall, and the mesh at the inflow plane. The node and element numbers for the model are given in Table 2. The Womersley parameter (defined in Sect. 4.2) is 2.0. This is based on the duration of one cardiac cycle (1 s) and the representative

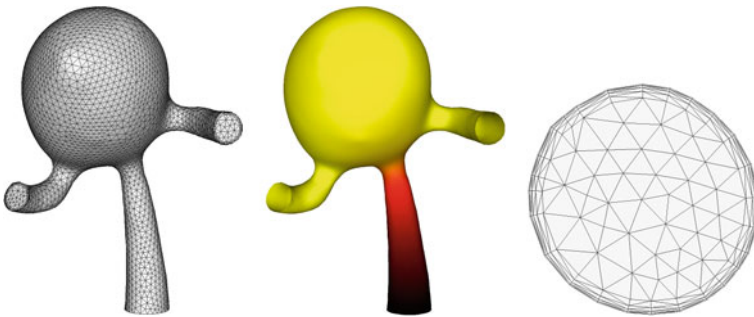


Fig. 7 Model-M6Acom. Fluid mechanics mesh at the lumen and outflow planes (*left*), thickness of the first layer of elements near the arterial wall (*middle*), and the mesh at the inflow plane (*right*). All pictures are from the starting point of our computation cycle. The *color range* represents a value range that increases from *light* to *dark*

Table 2 Model-M6Acom. Number of nodes and elements. Here *nn* and *ne* are number of nodes and elements, respectively

		M6Acom	
Structure	Volume	<i>nn</i>	17,574
		<i>ne</i>	11,650
	Interface	<i>nn</i>	5,858
		<i>ne</i>	5,825
Fluid	Volume	<i>nn</i>	33,040
		<i>ne</i>	192,112
	Interface	<i>nn</i>	3,528
		<i>ne</i>	6,996

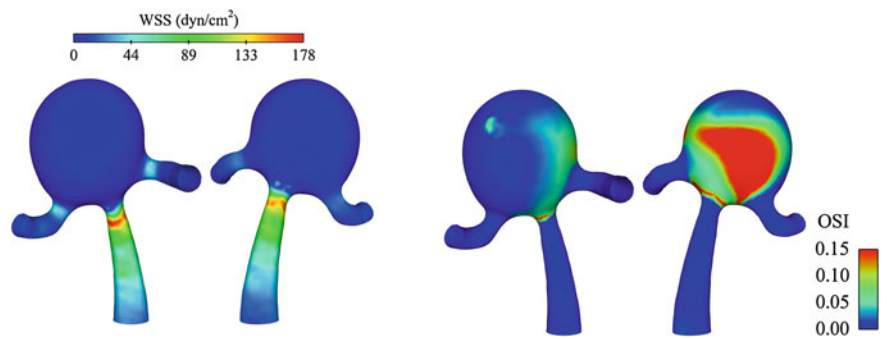


Fig. 8 Model-M6Acom. WSS when the volumetric flow rate is maximum and OSI

diameter is calculated from the inflow area corresponding to the shape when inflated to the average pressure.

The computations were carried out with the SSTFSI-TIP1 technique (see Remarks 8 and 16 in Tezduyar et al. 2011) and the SUPG test function option WTSA (see Remark 2 in Tezduyar et al. 2011). The stabilization parameters used are those given by Eqs. (12)–(18) in Tezduyar et al. (2011). The SSP option is used fully (see Remarks 21 and 22 in Tezduyar et al. 2011). The time-step size is 3.333×10^{-3} s. The number of nonlinear iterations per time step is 6. The number of GMRES iterations per nonlinear iteration for the fluid + structure block was chosen such that mass balance is satisfied to within at most 5 % for each case. The number of GMRES iterations is 300, and this was sufficient for obtaining good mass balance. For all six nonlinear iterations the fluid scale is 1.0 and the structure scale is 100. For the mesh moving block the number of GMRES iterations is 30. Figure 8 shows the WSS when the volumetric flow rate is maximum and the OSI. The OSI is calculated with the technique that excludes rigid-body rotations from the calculation (see Sect. 2.3).

7 Concluding Remarks

We presented an overview of the special techniques developed earlier by the T★AFSM for FSI modeling of patient-specific cerebral aneurysms. The core techniques are the DSD/SST and SSTFSI methods. The special FSI techniques developed in conjunction with the core techniques include (a) techniques for calculating an EZP geometry, (b) a special mapping technique for specifying the inflow velocity profile, (c) techniques for using variable arterial wall thickness, (d) techniques for building layers of refined fluid mechanics mesh near the arterial walls, (e) pre-FSI computation techniques that improve the convergence of the FSI computations, (f) techniques for calculation of the WSS and OSI, and (g) arterial-surface extraction and boundary condition techniques. With results from earlier computations carried out by the T★AFSM, we demonstrated how these techniques work. We also presented the special arterial FSI techniques developed and implemented very recently by the T★AFSM and the computational results obtained with these techniques. Overall, this review article shows that the space–time arterial FSI techniques developed by the T★AFSM can deal effectively with the computational challenges involved in arterial fluid mechanics problems.

Acknowledgments This work was supported in part by a seed grant from the Gulf Coast Center for Computational Cancer Research funded by John & Ann Doerr Fund for Computational Biomedicine. It was also supported in part by the Rice Computational Research Cluster funded by NSF Grant CNS-0821727. The 3DRA research at the Memorial Hermann Hospital University of Texas Medical School at Houston was supported by generous a funding from the Weatherhead Foundation. We thank Dr. Ryo Torii (University College London) for the inflow velocity data used in the computations and the arterial geometry used in [Sect. 6.1](#).

References

- Bazilevs Y, Hsu M-C, Benson D, Sankaran S, Marsden A (2009) Computational fluid–structure interaction: methods and application to a total cavopulmonary connection. *Comput Mech* 45:77–89
- Bazilevs Y, Hsu M-C, Zhang Y, Wang W, Kvamsdal T, Hentschel S, Isaksen J (2010) Computational fluid–structure interaction: methods and application to cerebral aneurysms. *Biomech Model Mechanobiol* 9:481–498
- Brooks AN, Hughes TJR (1982) Streamline upwind/Petrov–Galerkin formulations for convection dominated flows with particular emphasis on the incompressible Navier–Stokes equations. *Comput Methods Appl Mech Eng* 32:199–259
- Frank O (1899) Die grundform des arteriellen pulses. *Zeitung fur Biologie* 37:483–586
- Green AE, Naghdi PM (1976) A derivation of equations for wave propagation in water of variable depth. *J Fluid Mech* 78:237–246

- Huang H, Virmani R, Younis H, Burke AP, Kamm RD, Lee RT (2001) The impact of calcification on the biomechanical stability of atherosclerotic plaques. *Circulation* 103:1051–1056
- Hughes TJR, Liu WK, Zimmermann TK (1981) Lagrangian–Eulerian finite element formulation for incompressible viscous flows. *Comput Methods Appl Mech Eng* 29:329–349
- Johnson AA, Tezduyar TE (1994) Mesh update strategies in parallel finite element computations of flow problems with moving boundaries and interfaces. *Comput Methods Appl Mech Eng* 119:73–94
- McPhail T, Warren J (2008) An interactive editor for deforming volumetric data. *International conference on biomedical engineering 2008*, Singapore, pp 137–144
- Saad Y, Schultz M (1986) GMRES: a generalized minimal residual algorithm for solving nonsymmetric linear systems. *SIAM J Sci Stat Comput* 7:856–869
- Takizawa K, Brummer T, Tezduyar TE, Chen PR (2012) A comparative study based on patient-specific fluid–structure interaction modeling of cerebral aneurysms. *J Appl Mech* 79:010908
- Takizawa K, Christopher J, Tezduyar TE, Sathe S (2010a) Space–time finite element computation of arterial fluid–structure interactions with patientspecific data. *Int J Numer Methods Biomed Eng* 26:101–116
- Takizawa K, Moorman C, Wright S, Christopher J, Tezduyar TE (2010b) Wall shear stress calculations in space–time finite element computation of arterial fluid–structure interactions. *Comput Mech* 46:31–41
- Takizawa K, Moorman C, Wright S, Purdue J, McPhail T, Chen PR, Warren J, Tezduyar TE (2011) Patient-specific arterial fluid–structure interaction modeling of cerebral aneurysms. *Int J Numer Meth Fluids* 65:308–323
- Taylor CA, Hughes TJR, Zarins CK (1998) Finite element modeling of three-dimensional pulsatile flow in the abdominal aorta: relevance to atherosclerosis. *Ann Biomed Eng* 158:975–987
- Tezduyar T, Aliabadi S, Behr M, Johnson A, Mittal S (1993) Parallel finite-element computation of 3D flows. *Computer* 26(10):27–36
- Tezduyar TE (1992) Stabilized finite element formulations for incompressible flow computations. *Adv Appl Mech* 28:1–44
- Tezduyar TE (2004) Finite element methods for fluid dynamics with moving boundaries and interfaces. In: Stein E, Borst RD, Hughes TJR (eds) *Encyclopedia of computational mechanics*, vol 3: Fluids, Chap. 17. John Wiley & Sons, New York
- Tezduyar TE, Cragin T, Sathe S, Nanna B (2007a) FSI computations in arterial fluid mechanics with estimated zero-pressure arterial geometry. In: Onate E, Garcia J, Bergan P, Kvamsdal T (eds) *Marine 2007*. CIMNE, Barcelona
- Tezduyar TE, Sathe S (2007) Modeling of fluid–structure interactions with the space–time finite elements: Solution techniques. *Int J Numer Meth Fluids* 54:855–900
- Tezduyar TE, Sathe S, Cragin T, Nanna B, Conklin BS, Pausewang J, Schwaab M (2007b) Modeling of fluid–structure interactions with the space–time finite elements: arterial fluid mechanics. *Int J Numer Meth Fluids* 54:901–922
- Tezduyar TE, Sathe S, Keedy R, Stein K (2006) Space–time finite element techniques for computation of fluid–structure interactions. *Comput Methods Appl Mech Eng* 195:2002–2027
- Tezduyar TE, Sathe S, Schwaab M, Conklin BS (2008) Arterial fluid mechanics modeling with the stabilized space–time fluid–structure interaction technique. *Int J Numer Meth Fluids* 57:601–629
- Tezduyar TE, Schwaab M, Sathe S (2007c) Arterial fluid mechanics with the sequentially-coupled arterial FSI technique. In: Onate E, Papadarakakis M, Schrefler B (eds) *Coupled problems 2007*. CIMNE, Barcelona

- Tezduyar TE, Schwaab M, Sathe S (2009) Sequentially-coupled arterial fluid–structure interaction (SCAFSI) technique. *Comput Methods Appl Mech Eng* 198:3524–3533
- Tezduyar TE, Takizawa K, Brummer T, Chen PR (2011) Space–time fluid–structure interaction modeling of patient-specific cerebral aneurysms. *Int J Numer Methods Biomed Eng* 27:1665–1710
- Tezduyar TE, Takizawa K, Moorman C, Wright S, Christopher J (2010) Multiscale sequentially-coupled arterial FSI technique. *Comput Mech* 46:17–29
- Torii R, Oshima M, Kobayashi T, Takagi K, Tezduyar TE (2004) Influence of wall elasticity on image-based blood flow simulation. *Jpn Soc Mech Eng J A* 70:1224–1231 (in Japanese)
- Torii R, Oshima M, Kobayashi T, Takagi K, Tezduyar TE (2011) Influencing factors in image-based fluid–structure interaction computation of cerebral aneurysms. *Int J Numer Meth Fluids* 65:324–340
- Womersley JR (1955) Method for the calculation of velocity, rate of flow and viscous drag in arteries when the pressure gradient is known. *J Physiol* 127:553–563

Visualization and Simulation of Complex Flows in
Biomedical Engineering

Lima, R.; Imai, Y.; Ishikawa, T.; Oliveira, V. (Eds.)

2014, VIII, 240 p. 111 illus., Hardcover

ISBN: 978-94-007-7768-2